

Structure-Dynamics Correlation and Its Link to Fragility and Dynamic Heterogeneity

Mohit Sharma,^{1,2} Srikanth Sastry,³ and Sarika Maitra Bhattacharyya^{1,2, a)}

¹⁾*Polymer Science and Engineering Division, CSIR-National Chemical Laboratory, Pune-411008, India*

²⁾*Academy of Scientific and Innovative Research (AcSIR), Ghaziabad 201002, India*

³⁾*Theoretical Sciences Unit and School of Advanced Materials, Jawaharlal Nehru Centre for Advanced Scientific Research, Jakkur Campus, Bengaluru 560064, Karnataka, India*

Understanding the connection between structure, dynamics, and fragility (the rate at which relaxation times grow with decreasing temperature) is central to unraveling the glass transition. Fragility is often linked to dynamic heterogeneity, and thus it is commonly assumed that if structure influences dynamics, more fragile systems should exhibit stronger structure–dynamics correlations. In this study, we test the generality of this assumption using three model systems: Lennard-Jones (LJ) and Weeks–Chandler–Andersen, where fragility is tuned via density, and a modified LJ (q, p) system, where potential softness is changed to vary fragility. We employ a structural order parameter derived from the mean-field caging potential and analyze energy barriers at both macroscopic and microscopic levels. While the macroscopic slope of the energy barrier, suitably defined, correlates with fragility, no consistent correlation is found for the microscopic energy barriers. Instead, the latter shows a strong correlation with an independently computed structure–dynamics measure obtained from isoconfigurational ensemble. Surprisingly, the two systems with the highest structure–dynamics correlation, LJ at $\rho = 1.1$ and the (8, 5) model, are respectively the least and most fragile within their classes. These systems exhibit broad mobility distributions, bimodal displacement profiles, and high non-Gaussian parameters, all indicative of dynamic heterogeneity. However, their dynamic susceptibilities remain low, suggesting a decoupling between spatial correlation and temporal heterogeneity. Both systems lie in the enthalpy-dominated regime and are near the spinodal, suggesting mechanical instability as a source of heterogeneity. These findings challenge the conventional linkage among fragility, heterogeneity, and structure–dynamics correlation.

I. INTRODUCTION

The behaviour of supercooled liquids near the glass transition is characterised by a dramatic slowing down in dynamics without any obvious structural transition^{1–5}. The rapidity with which the relaxation time increases with decreasing temperature is quantified in terms of the fragility parameter⁶. Fragile liquids show a super-Arrhenius increase in relaxation time, while strong liquids follow an Arrhenius behaviour⁷.

One of the hallmarks of supercooled liquids is dynamic heterogeneity, the presence of regions with significantly different mobilities. Traditionally, this heterogeneity has been linked to fragility: more fragile systems tend to exhibit stronger dynamic heterogeneity^{2,7–12}. This link is often assessed through quantities like the four-point dynamic susceptibility, χ_4 , which captures spatial correlations in particle dynamics^{13,14}.

Although, as discussed in the literature, the glass transition and the rapid growth of the dynamics happens without substantial structural change^{1,4}, studies have shown that structure does indeed contribute to the dynamics, and small changes in structure can lead to large changes in other quantities like entropy which eventu-

ally strongly effects the dynamics^{15–17}. There have also been studies trying to understand the structural origin of dynamical heterogeneity^{18–21}. Among these studies, the machine learning study expressing the structural order by a softness parameter¹⁹ and the microscopic study involving some of us expressing the structural order in terms of the depth of a mean field caging potential^{20,22} sought to directly connect local structure to the local dynamics, in addition to investigating the global structure-dynamics correlation. For a fragile system, super-Arrhenius growth in the relaxation time implies a large change in the activation energy. It was suggested that the slope in the activation energy obtained from the macroscopic dynamics, when plotted as a function of the inverse depth of the caging potential, is high for more fragile liquids²⁰. In a later study involving the machine learned softness parameter, it was shown that the slope of the activation energy obtained from microscopic dynamics, when plotted against the ML softness, increases with fragility²³. A higher slope indicates that even small variations in the order parameter can lead to significant changes in the energy barrier and dynamics, reflecting a stronger coupling between structure and dynamics. Thus, these studies suggested that for a more fragile system, the structure-dynamics correlation is stronger, both macroscopically and microscopically.

Our goal in this study is to understand how generic this statement is. To do that, we take three different

^{a)} Electronic mail: mb.sarika@ncl.res.in

sets of systems and vary fragility by changing different properties. We take a system interacting via the attractive Lennard Jones (LJ) potential and its repulsive counterpart, the Weeks-Chandler-Andersen(WCA) potential, and vary their fragility by changing the density^{16,24}. We also vary the stepness of an attractive LJ-like potential and vary the fragility, which we refer to as the modified LJ (q, p) system consisting of (12, 11), (12, 6) and (8, 5) models (where the pairs of integers refer to the exponent of the repulsive and attractive interactions)^{25,26}. This way, we have both attractive and repulsive potentials and also systems where the fragility is varied without changing the density.

We find that there is no consistent correlation between fragility and the slope of the activation energy barrier. However, the latter does correlate well with a complementary measure of structure-dynamics correlation, as obtained from isoconfigurational ensemble simulations. Notably, two systems, LJ at $\rho = 1.1$ and (8, 5), exhibit the highest structure-dynamics correlation, despite having very different fragility values. What is striking is that both systems also display a broad distribution of particle mobilities, a distinct double-peak in the logarithmic displacement distribution, and large values of the non-Gaussian parameter but small values of four-point dynamic susceptibility. We also find that these two systems are in the enthalpy-dominated regime and very close to the spinodal line where it is known that dynamic heterogeneity may arise due to mechanical instability and growing fluctuations²⁷.

These findings lead us to emphasize a critical distinction: dynamic heterogeneity is a broader concept than what is captured by χ_4 which quantifies spatial correlations in particle motion. Dynamic heterogeneity also includes the distribution and variability of individual particle mobilities, which can arise due to different reasons and can exist even in the absence of significant spatial correlations. Thus, whereas χ_4 highlights cooperative dynamics, other measures, such as the van Hove correlation function, the non-Gaussian parameter and mobility distributions from isoconfigurational runs—reflect heterogeneity in a more general sense.

This insight is significant because it challenges the commonly held assumption that fragility, dynamic heterogeneity, and structure-dynamics correlation should be universally connected. Instead, our results point to a more nuanced picture, where distinct types of heterogeneity may dominate under different conditions, and where strong structure-dynamics correlation can arise from mechanisms not directly tied to fragility.

The rest of the paper is organized as follows. Section II describes the simulation details, while Section III outlines the methodology. Section IV presents the observations and results. Finally, Section V provides the conclusions. In addition, the paper includes four appendixes that provide supplementary information.

II. SIMULATION DETAILS

A. Simulation Details for the LJ and WCA Systems

The first two classes of systems we study are the 3-dimensional Kob-Andersen model for glass-forming liquid, which is a binary mixture (80:20) of Lennard-Jones (LJ) particles²⁸ and its repulsive counterpart Weeks-Chandler-Andersen potential (WCA)²⁹. The interaction between the particles i and j , where $i, j = A, B$ (the type of the particles), is given by

$$U_{ij}(r) = \begin{cases} U_{ij}^{(LJ)}(r; \sigma_{ij}, \epsilon_{ij}) & r \leq r_{ij}^{(c)} \\ -U_{ij}^{(LJ)}(r_{ij}^{(c)}; \sigma_{ij}, \epsilon_{ij}), & r > r_{ij}^{(c)}, \end{cases} \quad (1)$$

where $U_{ij}^{(LJ)}(r) = 4\epsilon_{ij}[(\sigma_{ij}/r)^{12} - (\sigma_{ij}/r)^6]$, r is the distance between particles i and j and σ_{ij} is the effective diameter of the particle and $r_{ij}^{(c)} = 2.5\sigma_{ij}$ for LJ and for the WCA system $r_{ij}^{(c)}$ is the position of minima of $U_{ij}^{(LJ)}(r)$.

The length, temperature, and time are given in units of σ_{AA} , ϵ_{AA}/k_B , $(m\sigma_{AA}^2/\epsilon_{AA})^{1/2}$, respectively. We use $\sigma_{AA} = 1.0$, $\sigma_{AB} = 0.8$, $\sigma_{BB} = 0.88$, $\epsilon_{AA} = 1.0$, $\epsilon_{AB} = 1.5$, $\epsilon_{BB} = 0.5$, $m_A = m_B = 1$ and Boltzmann constant $k_B = 1$.

We have performed MD simulation (using the LAMMPS package³⁰), we have used periodic boundary conditions and Nosé-Hoover thermostat with integration timestep 0.005τ . The time constants for Nosé-Hoover thermostat are taken to be 100 timesteps. We worked with 4 different total number density i.e. $\rho = 1.1, 1.2, 1.4, 1.6$ for both systems, where V is the system volume, and $N=4000$ is the total number of particles.

B. Simulation Details for the (q, p) Models

We also investigate a series of binary mixtures in which particles interact *via* a modified Lennard-Jones-type potential²⁵ defined as:

$$U_{ij}(r) = \begin{cases} \epsilon_{ij} \left[\left(\frac{r_{ij}^{\min}}{r} \right)^q - \left(\frac{r_{ij}^{\min}}{r} \right)^p \right] & r < r_c^{ij} \\ +c_{1,ij}r^2 + c_{2,ij}, & r \geq r_c^{ij} \end{cases} \quad (2)$$

Here, $r_{ij}^{\min} = 2^{1/6}\sigma_{ij}$ is the position of the potential minimum, and the correction terms $c_{1,ij}$ and $c_{2,ij}$ are chosen such that the potential and its derivative vanish smoothly at the cutoff radius $r_c^{ij} = 2.5\sigma_{ij}$:

$$U_{ij}(r_c^{ij}) = 0, \quad \left. \frac{dU_{ij}}{dr} \right|_{r=r_c^{ij}} = 0.$$

We consider three models denoted as (12, 11), (12, 6), and (8, 5), corresponding to exponent pairs $(q, p) = (12, 11)$, $(12, 6)$, and $(8, 5)$, respectively. The parameters σ_{ij} , ϵ_{ij} , and the units of length, temperature, and time are the same as defined for the LJ and WCA systems. Molecular dynamics simulations were performed using the LAMMPS package³⁰. A cubic box with periodic boundary conditions was used with a Nosé-Hoover thermostat. The integration timestep was set to 0.005τ . The thermostat time constant was 100 timesteps. The total number of particles was $N = 4000$, and the number density was fixed at $\rho = N/V = 1.2$.

III. METHODOLOGY

A. Structural order parameter

To quantify the static structure in glassy systems, we analyze the Structural Order Parameter (SOP) at both macroscopic and microscopic levels. The SOP characterizes the depth of the mean-field caging potential experienced by a particle due to its surrounding neighbors and is derived from the Ramakrishnan-Yussouff free energy functional³¹. We define the macroscopic SOP as $(\beta\Phi)^{-1}$ and the microscopic SOP as $(\beta\phi)^{-1}$ throughout this study. The effective caging potential at zero displacement is computed as

$$\beta\Phi = -\rho \int dr \sum_{uv} C_{uv}(r) x_u x_v g_{uv}(r), \quad (3)$$

where ρ is the number density, and x_u, x_v are the mole fractions of species u and v , respectively.

The radial distribution function $g_{uv}(r)$ is defined as³²

$$g_{uv}(r) = \frac{1}{4\pi r^2 \rho_v N_u} \left\langle \sum_{i=1}^{N_u} \sum_{j=1}^{N_v} \delta(r - |\mathbf{r}_i^u - \mathbf{r}_j^v|) \right\rangle, \quad (4)$$

where ρ_v is the number density of species v , N_u and N_v are the number of particles of species u and v , respectively, and the angular brackets denote an ensemble average over configurations.

$C_{uv}(r)$ is the direct correlation function which for the present study is approximated by using the Hypernetted Chain (HNC) closure relation³²:

$$C_{uv}(r) = -\beta U_{uv}(r) + (g_{uv}(r) - 1) - \ln g_{uv}(r), \quad (5)$$

where $U_{uv}(r)$ is the pairwise interaction potential between particles of species u and v , and $\beta = 1/(k_B T)$ is the inverse thermal energy.

At the microscopic level, the effective caging potential experienced by particle i of type u is given by

$$\beta\phi_u^i = -\rho \int dr \sum_v x_v C_{uv}^i(r) g_{uv}^i(r), \quad (6)$$

where ρ is the number density, $C_{uv}^i(r)$ is the local direct correlation function, and $g_{uv}^i(r)$ is the local radial distribution function for particle i .

To compute $g_{uv}^i(r)$, we employ a Gaussian smoothing scheme³³:

$$g_{uv}^i(r) = \frac{1}{4\pi\rho r^2} \sum_j \frac{1}{\sqrt{2\pi\delta^2}} \exp\left(-\frac{(r - r_{ij})^2}{2\delta^2}\right), \quad (7)$$

where r_{ij} is the distance between particle i and particle j , and $\delta = 0.09\sigma_{AA}$ is the Gaussian width parameter. This smoothing technique provides a continuous and differentiable estimate of the local radial distribution function, mitigating the noise associated with discrete binning methods.

B. Entropy and local energy

The two-body excess entropy at the particle level for a binary system, corresponding to a particle i of type u , is computed as³⁴:

$$S_{u2}^i = -k_B \frac{\rho}{2} \sum_{v=1}^2 x_v \int_0^\infty \{g_{uv}^i(r) \ln g_{uv}^i(r) - g_{uv}^i(r) + 1\} dr, \quad (8)$$

where the local radial distribution function $g_{uv}^i(r)$ is calculated as described in Section III A.

Similarly, the local potential energy e_{uloc}^i for a particle i of type u is given by:

$$e_{uloc}^i = \frac{\rho}{2} \sum_{v=1}^2 x_v \int_0^\infty U_{uv}(r) g_{uv}^i(r) dr, \quad (9)$$

where the interaction potential $U_{uv}(r)$ has been defined in the simulation details section (Section II).

C. Relaxation time and Four-Point Susceptibility

The structural relaxation time, τ_α , is determined from the condition $q(t = \tau_\alpha) = 1/e$, where $q(t)$ denotes the time-dependent overlap function²⁵. It is defined as

$$q(t) = \frac{1}{N} \sum_{i=1}^N \omega(|\mathbf{r}_i(t) - \mathbf{r}_i(0)|), \quad (10)$$

where the indicator function $\omega(x)$ takes the value 1 if $0 \leq x \leq a$ and 0 otherwise. The choice of the cut-off parameter a is crucial, as it determines the sensitivity of the overlap function to particle displacements. In this study, we set $a = 0.3$ to account for low-amplitude vibrational motion such that particles undergoing only minor displacements are still considered to remain in the same position. This value is selected to be comparable to the mean squared displacement (MSD) observed in the

plateau regime, which separates the ballistic and diffusive regimes in the dynamics.

As discussed earlier, in supercooled liquids, the relaxation time grows rapidly with temperature. This growth can be described by the Vogel-Fulcher-Tammann (VFT) relation,³⁵

$$\tau_\alpha(T) = \tau_0 \exp\left(\frac{T_{VFT}}{K_{VFT}(T - T_{VFT})}\right), \quad (11)$$

where τ_0 is a prefactor, T_{VFT} is the temperature where the dynamics should diverge, and K_{VFT} is the kinetic fragility which quantifies how rapidly the relaxation time grows with temperature. A high value of K_{VFT} corresponds to a more fragile system, while a smaller value of K_{VFT} indicates a stronger liquid.

To quantify spatial correlations in mobility, we compute the four-point susceptibility $\chi_4(t)$, defined as the variance of the time-dependent overlap function³⁶ $q(t)$:

$$\chi_4(t) = N [\langle q^2(t) \rangle - \langle q(t) \rangle^2], \quad (12)$$

where N is the total number of particles. The peak of $\chi_4(t)$ identifies the time scale of maximum dynamic heterogeneity.

D. van Hove correlation Function and Non-Gaussian Parameter

The self-part of the van Hove correlation function^{32,37}, which gives the probability distribution of single-particle displacements is written as:

$$G_s(r, t) = \left\langle \frac{1}{N} \sum_{i=1}^N \delta(r - |\mathbf{r}_i(t) - \mathbf{r}_i(0)|) \right\rangle. \quad (13)$$

For systems in the high temperature regime, when the particle motion is homogeneous and diffusive, the van Hove correlation function is Gaussian. However, at the low temperature regime, due to heterogeneity in particle motion, the van Hove correlation function becomes non-Gaussian and it develops a tail which is best visualised in the probability distribution of logarithmic displacements³⁸, $P(\log_{10} \delta r)$, which is defined as:

$$P(\log_{10} \delta r) = \ln(10) 4\pi \delta r^3 G_s(\delta r, t). \quad (14)$$

This representation emphasizes both mobile and immobile particle populations and is particularly useful for identifying the broad, often bimodal, displacement distributions observed at the α -relaxation time in dynamically heterogeneous systems.

To measure the deviation of the particle displacement distribution from Gaussian, we use the non-Gaussian parameter³⁹, $\alpha_2(t)$, defined as:

$$\alpha_2(t) = \frac{3\langle \delta r^4(t) \rangle}{5\langle \delta r^2(t) \rangle^2} - 1, \quad (15)$$

where $\langle \delta r^n(t) \rangle$ denotes the n -th moment of the particle displacement distribution at time t . A higher value of $\alpha_2(t)$ indicates an increased dynamic heterogeneity and non-Gaussian behavior in the displacement distribution.

IV. RESULTS

As discussed in the Introduction, in this study we work with three different sets of systems, i) the attractive LJ potential at different densities ii) the repulsive WCA potential, at different densities^{16,24}, iii) modified LJ (q, p) system consisting of (12, 11), (12, 6) and (8, 5), systems-LJ-like potential where the steepness of the potential is varied^{25,26}, and vary fragility by changing different properties like the density and the steepness of the potential. While describing the results in all figures, we use a consistent color and symbol scheme to represent increasing fragility for each set: black circles for the least fragile systems, followed by red squares, green up-triangles, and blue down-triangles for progressively more fragile systems.

A. The temperature and SOP dependence of the energy barrier and its correlation with fragility

We can describe the macroscopic energy barrier, $\Delta E^{ma} = T * \ln(\tau_\alpha/\tau_0)$, where τ_α is the α -relaxation time of the systems as obtained from the overlap function (Section III C). τ_0 is a prefactor. In Fig.1(left panels), we plot the macroscopic energy barrier as a function of inverse macroscopic SOP, $\beta\Phi$, for the three different sets of systems. We can also obtain the energy barrier from the microscopic motion of particles. This is a standard procedure^{19,22}, and the details are given in Appendix II. We can write the probability of a particle with a certain value of the inverse SOP to be a fast moving particle as, $P_R(\beta\phi) = P_0(\beta\phi) \exp[-\Delta E(\beta\phi)/T]$. Here $\Delta E(\beta\phi)$ is the energy barrier for particles having the value of the inverse microscopic order parameter $\beta\phi$ (given in Eq.3). The microscopic energy barriers thus obtained are plotted against the inverse microscopic per particle level SOP, $\beta\phi$ (right panels of Fig.2). We find that the rate of growth of both the macroscopic and the microscopic energy barriers show a similar trend. For the LJ and the WCA systems, we find that as the fragility of the systems increases, the average slope of the energy barrier increases. In a previous study involving some of us,²⁰ it was shown that the energy barrier as a function of the inverse SOP can be fitted in a straight line $\Delta E^{ma} = A + B * \beta\Phi$ where A and B are system-specific fitting parameters. This then suggests that the temperature dependence of the activation energy depends on the temperature dependence of the SOP. Thus, for strong liquids where the energy barrier is independent of temperature, it was shown that the parameter $B \rightarrow 0$ ²⁰ and the fact that the slope B increases with fragility is an expected result. A simi-

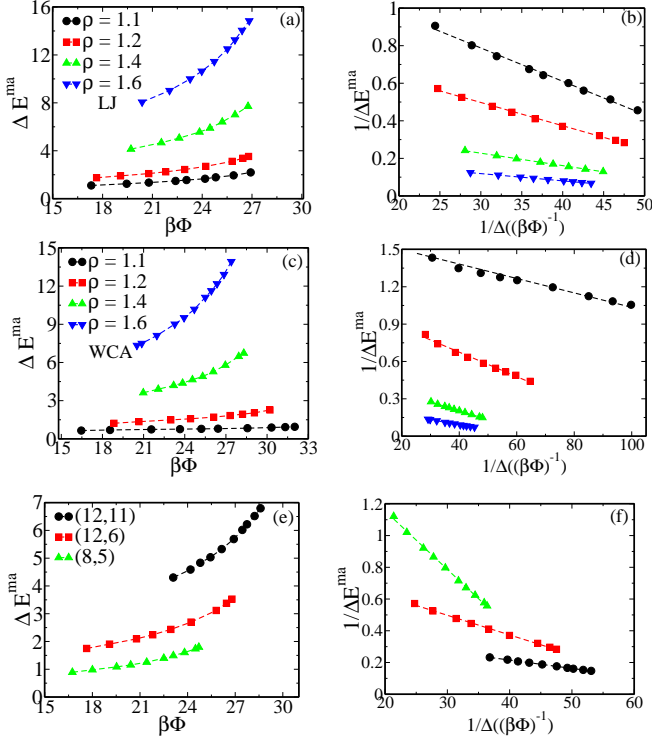


FIG. 1: **Left Panels:** Macroscopic energy barrier, ΔE^{ma} , plotted against the inverse macroscopic structural order parameter, $\beta\Phi$, for three sets of systems: (a)LJ and (c)WCA, each examined at four different densities, and (e) modified LJ (q, p) system. **Right Panels:** The inverse activation energy $1/\Delta E^{ma}$ plotted against $1/\Delta((\beta\Phi)^{-1})$ for the same systems. The slope of the linear fits yields the B'/A' values used in the fragility analysis (see Fig.4). The color coding in the right panels matches that of the left panels.

lar observation was also made in the ML studies, where it was shown that the slope of the microscopic energy barrier against the ML softness parameter increases with fragility²³. However, the behavior appears to be completely reversed when we consider the set of modified LJ, (q, p) systems where the fragility is varied by changing the steepness of the potential. In this case, the slope of both the macroscopic and microscopic energy barriers is lowest for the (8, 5) system—the most fragile—and highest for the (12, 11) system—the least fragile. This finding challenges the commonly held assumption^{20,23} that the most fragile system should exhibit the steepest slope in the energy barrier versus the SOP, raising the question of whether this relationship is truly generic.

Note that this analysis depends on the order parameter we choose, and the fragility in terms of the order parameter can be different from that in terms of temperature. First, we present the temperature dependence of the SOP. Similar to earlier studies^{20,22}, we find that for all the systems the SOP, at macroscopic level, $\langle(\beta\Phi)^{-1}\rangle$

and microscopic level, $\langle(\beta\phi)^{-1}\rangle$ are linearly proportional to the temperature (right panel of Fig.2). Although the value of the order parameter at the macroscopic and microscopic levels is different, which is expected (as elaborated in Appendix I), their temperature dependences are similar. Both at the macroscopic and the microscopic levels, the SOP is linear with T and can be fitted to the equations $(\beta\Phi)^{-1} = (\beta\Phi_0)^{-1} + \gamma T$, and $\langle(\beta\phi)^{-1}\rangle = \langle(\beta\phi_0)^{-1}\rangle + \gamma' T$ where γ and γ' are the corresponding slopes (given in Table I). $(\beta\Phi_0)^{-1}$ and $\langle(\beta\phi_0)^{-1}\rangle$ are the values of the macroscopic and average microscopic SOP, at $T=0$, respectively. We find that the values of the slopes γ and γ' are not identical but similar, which can be expected as both come from the temperature evolution of the radial distribution function.

We have redefined our order parameter at the macroscopic and microscopic level as,

$$\begin{aligned}\Delta((\beta\Phi)^{-1}) &= (\beta\Phi)^{-1} - (\beta\Phi_0)^{-1} = \gamma T, \\ \Delta(\langle(\beta\phi)^{-1}\rangle) &= \langle(\beta\phi)^{-1}\rangle - \langle(\beta\phi_0)^{-1}\rangle = \gamma' T,\end{aligned}\quad (16)$$

We next investigate the fragility of the systems both as a function of temperature, given by Eq.11, and also as a function of $\Delta((\beta\Phi)^{-1})$, which can be represented by the following VFT expression³⁵,

$$\tau_\alpha(\Delta((\beta\Phi)^{-1})) = \tau_0 \exp\left(\frac{\Delta((\beta\Phi)^{-1}_{VFT})}{K_{VFT}(\Delta((\beta\Phi)^{-1}) - \Delta((\beta\Phi)^{-1}_{VFT}))}\right) \quad (17)$$

Here $\Delta((\beta\Phi)^{-1}_{VFT})$ is the value of the order parameter at the VFT temperature. Note that Eq.17 can be written when we replace the temperature in Eq.11 by the SOP as given in Eq.16. In Fig.3, we present a master plot of the VFT fit for all the systems as a function of the SOP. The inset shows the corresponding plot as a function of temperature. The good data collapse in both representations confirms the validity of the equations (Eq.11 and Eq.17) and the consistency of the extracted VFT parameters, as listed in Table I. We find that the fragility in terms of the temperature and the SOP is the same.

We next investigate the temperature and SOP dependence of the barrier $\Delta E^{ma} = T \ln(\tau_\alpha/\tau_0)$ as predicted by the VFT expression. From the VFT expression, Eq.11 we can write,

$$\Delta E^{ma}/T = \frac{T_{VFT}}{K_{VFT}(T - T_{VFT})} \quad (18)$$

In the range away from T_{VFT} , we can expand $(1 - T_{VFT}/T)$ by Taylor expansion, and using the first-order approximation, we can write

$$\Delta E^{ma} \approx \frac{T_{VFT}}{K_{VFT}} + \frac{T_{VFT}^2}{K_{VFT}} \cdot \frac{1}{T} \quad (19)$$

This clearly shows that the slope of ΔE^{ma} is not directly proportional but inversely proportional to the fragility. For both the LJ and WCA systems, fragility increases with density, accompanied by a corresponding rise in T_{VFT} as the systems at higher densities operate in higher temperature regimes. This trend explains why we observe an increase in the slope, $\frac{T_{VFT}^2}{K_{VFT}}$

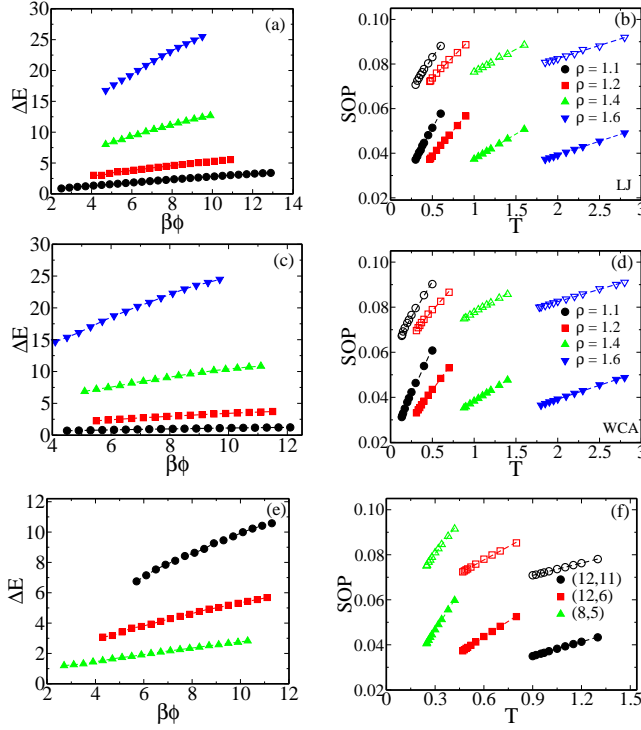


FIG. 2: **Left Panels:** Microscopic energy barrier, ΔE , versus the inverse microscopic structural order parameter, $\beta\phi$, for three sets of systems: (b) LJ and (d) WCA, each examined at four different densities, and (f) modified LJ (q, p) system. **Right Panels:** Temperature dependence of both the macroscopic structural order parameter, $(\beta\Phi)^{-1}$, (closed symbols) and the average microscopic structural order parameter $\langle(\beta\phi)^{-1}\rangle$, (open symbols) for the same systems. Dotted lines represent linear fits used to extract slope parameters for further analysis. The color coding in the left panels matches that of the right panels.

with increasing fragility. For the modified LJ (q, p) system the fragility is higher for the (8,5) system which has the lowest value of T_{VFT} and this is the reason even in the ΔE^{ma} vs $1/T$ plots the (8,5) system has the lowest slope (left panels of Fig.13 in the Appendix III). Interestingly the slope of $1/\Delta E^{ma}$ vs $1/T$ is the fragility (right panels of Fig.13 in Appendix III),

$$1/\Delta E^{ma} = \frac{K_{VFT}}{T_{VFT}} - K_{VFT} \cdot \frac{1}{T} \quad (20)$$

We next investigate the SOP dependence of ΔE^{ma} . In Eq.19 and Eq.20 if we replace T in terms of SOP (Eq.16) we can write,

$$\Delta E^{ma} \approx \frac{T_{VFT}}{K_{VFT}} + \gamma \cdot \frac{T_{VFT}^2}{K_{VFT}} \cdot \frac{1}{\Delta((\beta\Phi)^{-1})} = A + B \cdot \frac{1}{\Delta((\beta\Phi)^{-1})} \quad (21)$$

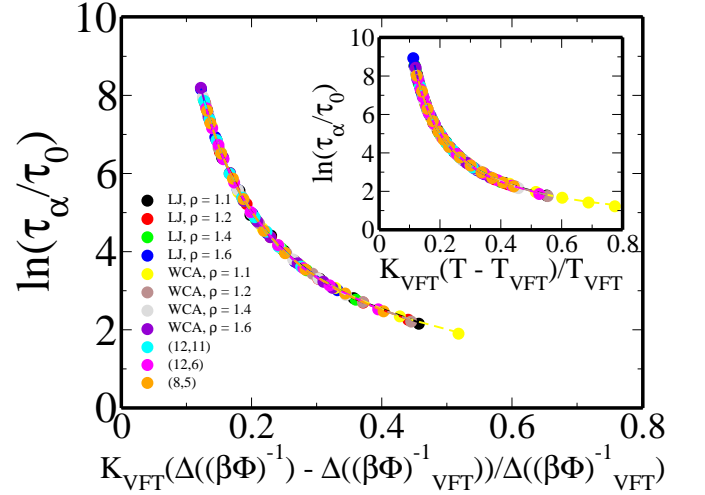


FIG. 3: Master plot of the VFT equation w.r.t SOP, (Eq.17) for all the systems—LJ and WCA at four different densities, and modified LJ (q, p) system. The inset displays the corresponding master of the VFT equation with respect to temperature T (Eq.11). The collapse of the data confirms the validity of the equations and the consistency of the extracted VFT parameters, as listed in Table I.

and

$$1/\Delta E^{ma} = \frac{K_{VFT}}{T_{VFT}} - \gamma \cdot K_{VFT} \cdot \frac{1}{\Delta((\beta\Phi)^{-1})} = A' + B' \cdot \frac{1}{\Delta((\beta\Phi)^{-1})} \quad (22)$$

From Eq.21 we get $A = \frac{T_{VFT}}{K_{VFT}}$ and $B = \gamma \cdot \frac{T_{VFT}^2}{K_{VFT}}$ and the slope is again not proportional to but inversely proportional to the fragility. Thus similar to the argument given for the temperature dependence of the energy barrier, we find that as shown in Fig.1(left panels) and Fig.2 (left panels) the slopes do not always follow fragility. In cases where it follows fragility, it is because for more fragile systems the T_{VFT} is higher. From Eq.22 we get that $A' = \frac{K_{VFT}}{T_{VFT}}$ and $B' = \gamma \cdot K_{VFT}$. Thus, similar to that observed in temperature dependence, the slope of $\frac{1}{\Delta E^{ma}}$ is proportional to fragility. However, in this case, there is this additional factor γ which describes the dependence of the SOP on the temperature.

Note that the temperature dependence of the energy barrier, ΔE^{ma} comes from the temperature dependence of the SOP, and the energy barrier has a temperature independent term. A similar observation can also be made for $\frac{1}{\Delta E^{ma}}$. The temperature independent term in the energy sets an energy scale. Thus, to understand the effect of change in the energy on the dynamics, we should scale the energy by its temperature independent value. We find from Eq.21 and Eq.22 that the slopes of both $\Delta E^{ma}/A$ and $1/(\Delta E^{ma} \cdot A')$ are the same and equal to $B/A = B'/A' = \gamma T_{VFT}$. The values of γ obtained from the temperature dependence of the macroscopic SOP (right panels in Fig.2) are given in Table I. We observe that γT_{VFT} varies linearly with the fragility parameter K_{VFT} across all three sets of systems, as demonstrated in Fig.4. Note that at the macroscopic level ΔE^{ma} as a function of

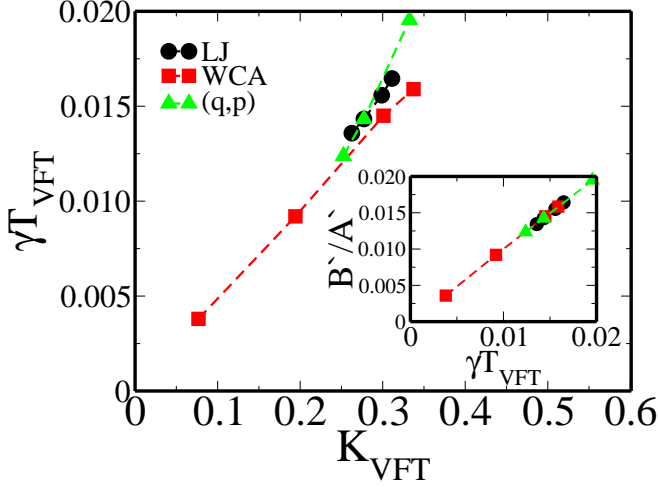


FIG. 4: The main panel displays γT_{VFT} plotted against K_{VFT} for three sets of systems: LJ, WCA, and modified LJ (q,p) system. Each set exhibits a clear linear relationship, indicating a consistent correlation between the parameters. **Inset:** The scaled slope of the macroscopic energy barrier plot, B'/A' , derived from the $1/\Delta E^{ma}$ versus $1/\Delta((\beta\Phi)^{-1})$ plot in the right panel of Fig.1, is plotted against γT_{VFT} . All data points lie on the $y = x$ line, demonstrating that the two quantities are numerically identical, validating our analysis.

SOP does not actually show a linear dependence (left panels of Fig.1) and Eq.21 is an approximate expression. However, as shown in the right panel of Fig.1, $1/\Delta E^{ma}$ as a function of SOP does show a linear behaviour validating Eq.22. Thus, we obtain the values of A' and B' from right panels in Fig.1 (given in Table.II in the Appendix III). In the inset of Fig.4 we also plot B'/A' against γT_{VFT} . We find that all the points fall on the $y=x$ line, thus confirming our analysis. The physical reason for γT_{VFT} being a good fragility metric needs further investigation.

Next we study the validity of the same analysis for the microscopic ΔE . In Fig.2(left panels) we plot the ΔE vs $1/\Delta((\beta\phi)^{-1})$. Notably, unlike at the macroscopic level where the energy barrier increases more than linearly with the structural order parameter(SOP) (left panels of Fig.1), at the microscopic level, ΔE as a function of SOP (left panels of Fig.2) exhibits a linear behavior. A similar linear trend is also seen in the ΔE vs. modified SOP plot (left panels of Fig.5). In the calculation of the microscopic energy barrier, it is assumed that the dynamics is given by P_R^{-1} (see Appendix II). The fact that ΔE^{ma} grows more strongly compared to ΔE can be attributed to the fact that P_R^{-1} is related to a shorter time dynamics which does not have the information of the cooperativity in the dynamics thus grows slower than τ_α , an observation previously reported by Tah et al²³. However, as discussed before, the approximate behaviour at the macroscopic and microscopic levels remains similar. For the LJ and the WCA system, we find that the rate of growth of the energy barriers follow the fragility, whereas for the modified LJ (q,p) system, the behaviour is the reverse. We next plot in Fig.5

TABLE I: Fitted values of the VFT temperature, T_{VFT} , and fragility, K_{VFT} , for various systems, obtained using Eq.11. The parameters γ and γ' represent the temperature dependence of our SOP (Eq.16) at macroscopic and microscopic levels respectively, (right panel of Fig.2). Note that (12,6) system is same as LJ at $\rho = 1.2$

System	T_{VFT}	K_{VFT}	γ	γ'
LJ, $\rho = 1.1$	0.197	0.262	0.068	0.056
LJ, $\rho = 1.2$	0.317	0.277	0.045	0.038
LJ, $\rho = 1.4$	0.697	0.298	0.022	0.020
LJ, $\rho = 1.6$	1.322	0.311	0.012	0.011
WCA, $\rho = 1.1$	0.047	0.076	0.081	0.062
WCA, $\rho = 1.2$	0.181	0.194	0.051	0.042
WCA, $\rho = 1.4$	0.613	0.300	0.023	0.021
WCA, $\rho = 1.6$	1.289	0.337	0.012	0.010
(12, 11)	0.590	0.252	0.020	0.018
(12, 6)	0.317	0.277	0.045	0.038
(8, 5)	0.174	0.332	0.111	0.095

(right panels) the scaled energy $\Delta E/A$, where the A is obtained by fitting the SOP dependence of the energy barrier to a linear form $\Delta E = A + B \cdot \frac{1}{\Delta((\beta\phi)^{-1})}$. According to our previous analysis, $B/A(micro)$, the slope of the scaled microscopic energy barrier should be equal to γT_{VFT} . However, as shown in Fig.6(a) that does not seem to be the case. In the inset of Fig.6(a) we also plot $B/A(micro)$ against K_{VFT} , and again no consistent trend is observed. This behaviour is in stark contrast to that of the macroscopic counterpart. The slope of the microscopic energy barrier varies significantly across systems and does not follow a universal trend. For instance, in the modified LJ (q,p) system $B/A(micro)$ appears to track both γT_{VFT} and K_{VFT} . In contrast, the WCA systems, which exhibit the largest variation in fragility, show almost no change in the $B/A(micro)$. Interestingly, for the LJ systems, the slope of the scaled microscopic energy barrier varies inversely with both γT_{VFT} and K_{VFT} .

Thus, although the macroscopic and microscopic energy barriers appear to exhibit qualitatively similar variation with the SOP, a more detailed analysis reveals key differences. The scaled slope of the energy barrier as a function of SOP quantifies how sensitively the barrier and therefore, the dynamics responds to structural changes. A higher slope indicates that even small variations in SOP lead to significant changes in the energy barrier and dynamics, reflecting a stronger coupling between structure and dynamics.

Accordingly, the macroscopic and microscopic energy barriers imply different strengths of structure-dynamics correlation. This discrepancy may originate from the nature of the analyses: macroscopic approaches average over many particles, thereby smoothing out local fluctuations and heterogeneities. In contrast, microscopic analysis preserves particle-level detail and captures spatially localised structural variations and dynamic heterogeneity. As a result, macroscopic models may overlook subtle but crucial features that govern dynamic behaviour.

To assess which perspective more accurately captures the structure-dynamics relationship, we next employ a complementary and direct measure of structure-dynamics correlation. The correlation between SOP and particle mobility, ob-

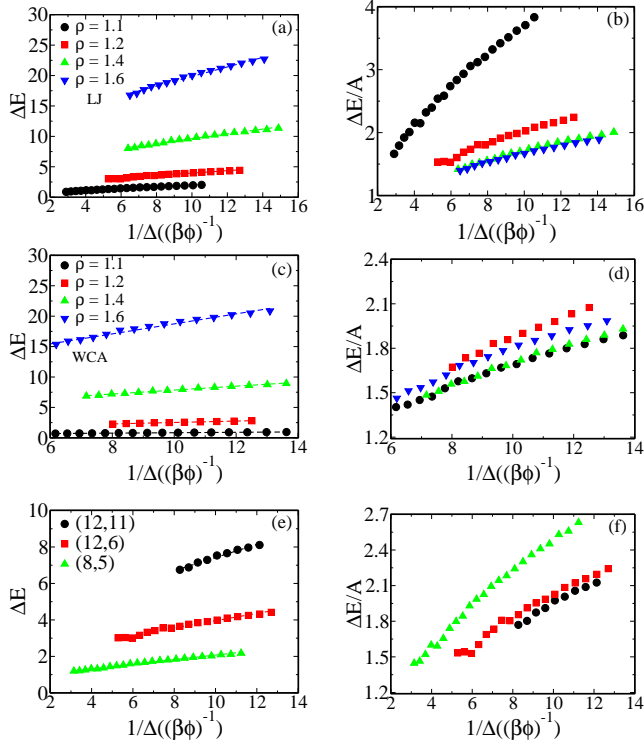


FIG. 5: **Left panels:** Microscopic energy barrier, ΔE , plotted as a function of inverse microscopic structural order parameter, $1/\Delta((\beta\phi)^{-1})$, for three sets of systems: (a)LJ and (c)WCA, each examined at four different densities, and (e) modified LJ (q,p) system. **Right panels:** Scaled microscopic energy barrier, $\Delta E/A$, plotted against $1/\Delta((\beta\phi)^{-1})$ for the same systems shown in the left panels. The colour coding in the right panels matches that of the left panels.

tained from isoconfigurational ensemble simulations.

B. Structure-Dynamics correlation via isoconfigurational study

As discussed before, in order to apply an independent method to study structure-dynamics correlation, we perform the study using isoconfiguration runs. This is a powerful technique which was proposed by Harrowell and co-workers¹⁸ to extract the effect of any structural order parameter on the dynamics. To enable a meaningful comparison across systems with different densities, we select temperatures such that the α -relaxation time is approximately the same for each system. The working temperatures used for comparing different densities are listed in Table III in Appendix IV. We then compute the Spearman rank correlation between the SOP at the initial time and the particle mobility measured at different times (Fig.7). As observed earlier by us⁴⁰ and also discussed in detail in the literature^{5,41–45}, the correlation between an order parameter and the dynamics when the order parameter is calculated at a single particle level is high at short

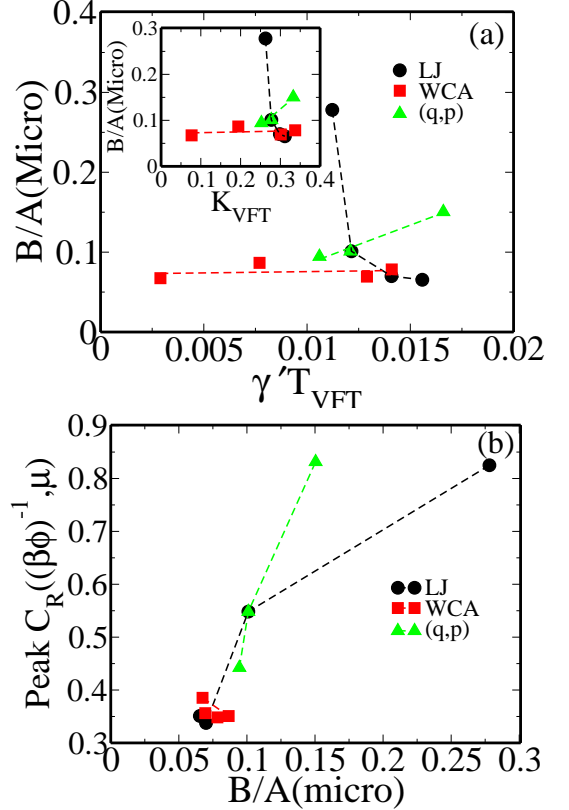


FIG. 6: (a) The main panel presents the scaled slope of the microscopic energy barrier plot, $B/A(\text{micro})$, obtained from the slope of the $\Delta E/A$ versus $1/\Delta((\beta\phi)^{-1})$ plot (right panel of Fig.5), plotted against $\gamma'T_{\text{VFT}}$ for three sets of systems: LJ, WCA, and modified LJ (q,p) system. The data exhibit distinct behaviours across the systems. **Inset:** $B/A(\text{micro})$ plotted against K_{VFT} shows a similar trend to the main plot, consistent with the linear relationship between $\gamma'T_{\text{VFT}}$ and K_{VFT} (demonstrated in Fig.4). (b) The peak value of the Spearman rank correlation between the coarse grained SOP and the dynamics, $C_R((\beta\phi)^{-1}, \mu)$, obtained from Fig.7, plotted against $B/A(\text{micro})$.

times and then drops at longer times. However, the correlation with coarse grained order parameter increases at long times. The coarse graining of a parameter X for the i^{th} particle, when coarse grained over a length scale L , is defined as $\bar{X}_i(L) = \sum_j X_j P(r_j - r_i) / \sum_j P(r_j - r_i)$, where $P(x) = \exp(-x/L)$, under the hypothesis that the influence of the neighbourhood decays exponentially with distance. Studies have shown that there is an optimal value of the coarse graining length where the correlation is maximum^{5,40–42,45}. The SOP is coarse-grained over this length, $L = 4$ for LJ, and modified LJ (q,p) system and $L = 3$ for WCA systems in such a way that it yields maximum correlation. Note that, as shown in the left panels of Fig.15 in Appendix IV, although the value of the correlation changes with L , the nature of the plot remains similar. Our analysis reveals that

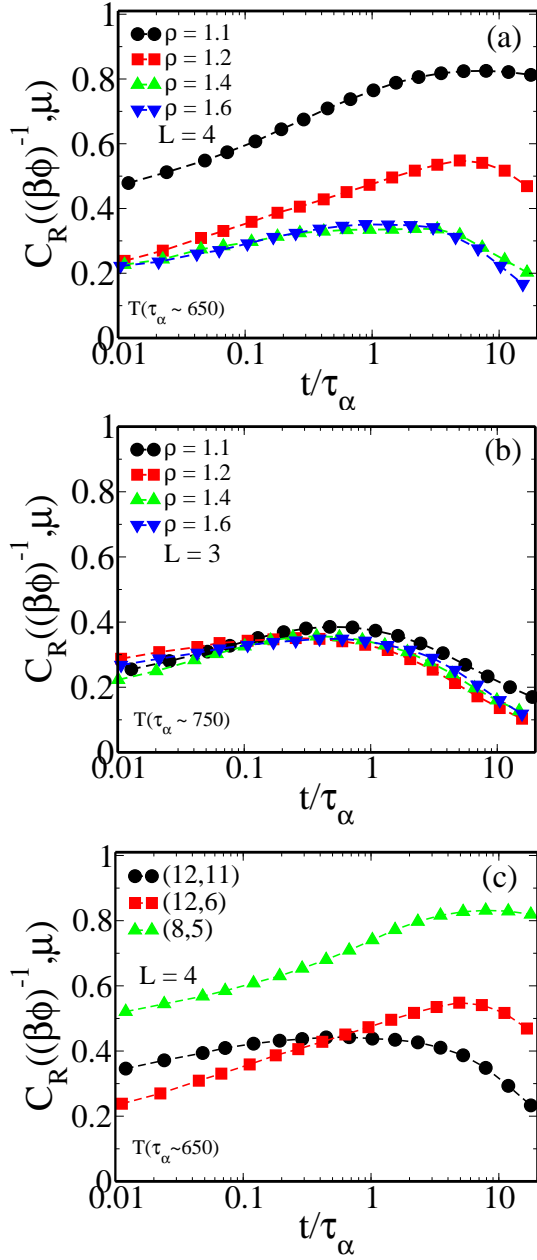


FIG. 7: Spearman rank correlation, $C_R((\beta\phi)^{-1}, \mu)$, between the coarse-grained structural order parameter, $(\beta\phi)^{-1}$, and particle mobility, μ , is plotted as a function of time scaled by the α -relaxation time (t/τ_α) for three sets of systems: (a) LJ system at four densities: with coarse-graining length $L = 4$; (b) WCA system at the four densities with $L = 3$; (c) modified LJ (q, p) system with $L = 4$.

the structure-dynamics correlation is not always related to fragility. However, we find a strong relationship between the structure-dynamics correlation and the slope of the scaled microscopic energy barrier across all three sets of systems (Fig.6(a)): i) For the LJ system, both the slope and the structure-dynamics correlation decrease with increasing fragility.

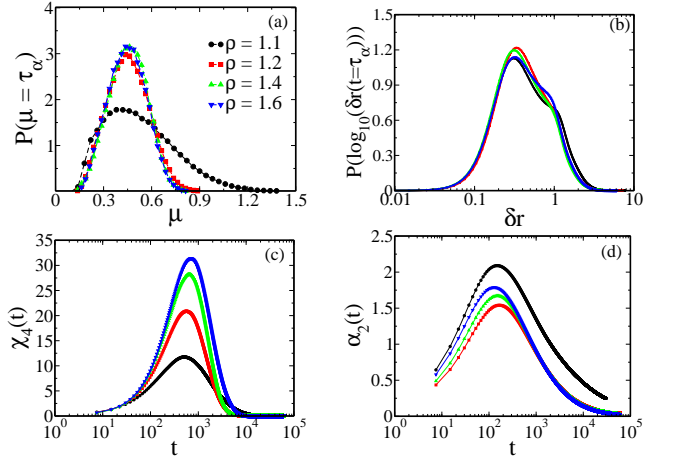


FIG. 8: Different measures of heterogeneity for the LJ systems (a) Distribution of particle mobilities at the α -relaxation time, obtained from isoconfigurational ensemble simulations. (b) Logarithmic distribution of single-particle displacements, $P(\log_{10}(\delta r(t = \tau_\alpha)))$, derived from standard simulation trajectories. (c) Four-point susceptibility, $\chi_4(t)$, plotted as a function of time. (d) Non-Gaussian parameter, $\alpha_2(t)$, plotted as a function of time. The system exhibiting the maximum structure-dynamics correlation ($\rho = 1.1$) is characterized by a broader $P(\mu)$, a bimodal $P(\log_{10}(\delta r(t = \tau_\alpha)))$, and a higher peak in $\alpha_2(t)$. The color coding in (b),(c),(d) matches that of (a).

ii) For the WCA system, despite exhibiting the largest variation in fragility, both the slope and the structure-dynamics correlation remain nearly constant and appear independent of fragility. iii) For the modified LJ (q, p) system, both the slope and the structure-dynamics correlation increase with fragility. Fig.6(b) shows the peak value of the structure-dynamics correlation C_R against the scaled microscopic energy barrier $B/A(\text{micro})$, which quantitatively underscores this observation.

These findings allow us to conclude that the slope of the scaled microscopic energy barrier is closely linked to the structure-dynamics correlation. In contrast, the slope of the scaled macroscopic energy barrier, given by γT_{VFT} does follow fragility but not the structure-dynamics correlation. This implies that the structure-dynamics correlation is not trivially connected to fragility. However, phenomenologically, fragility has been linked to dynamic heterogeneity, with more fragile systems typically exhibiting stronger heterogeneity in dynamics^{2,12}. This raises an important and open question: What fundamental mechanism governs the system dependent trends in structure-dynamics correlation, and how is this related to dynamic heterogeneity?

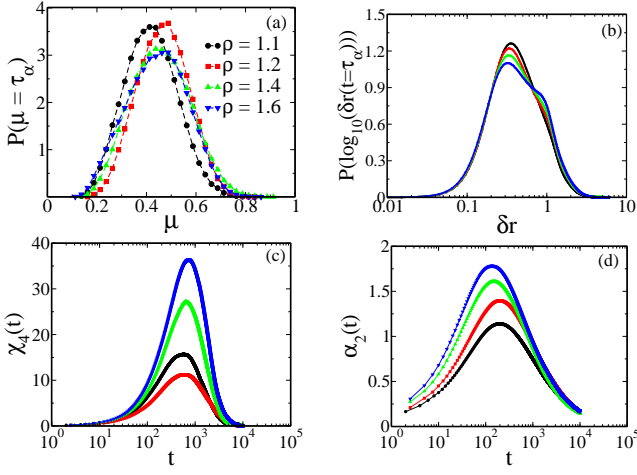


FIG. 9: Different measures of heterogeneity for the WCA systems (a) Distribution of particle mobilities at the α -relaxation time, obtained from isoconfigurational ensemble simulations. (b) Logarithmic distribution of single-particle displacements, $P(\log_{10}(\delta r(t = \tau_\alpha)))$, derived from standard simulation trajectories. (c) Four-point susceptibility, $\chi_4(t)$, plotted as a function of time. (d) Non-Gaussian parameter, $\alpha_2(t)$, plotted as a function of time. Across all densities, the system exhibits consistent trends in dynamic heterogeneity metrics, with structure-dynamics correlations remaining similar. The color coding in (b), (c), (d) matches that of (a).

C. Dynamic heterogeneity and structure-dynamics correlation

In the literature, dynamical heterogeneity is characterised using several complementary approaches. In this study, we employ the logarithm of the distribution of single-particle displacements at the α -relaxation time, expressed as, $P(\log_{10}(\delta r(t = \tau_\alpha))) = \ln(10)4\pi\delta r^3 G_s(\delta r, t)$ which is related to the self-part of the van Hove correlation function, $G_s(\delta r, t)$ ⁴⁶. In addition, we analyse two commonly used dynamical measures: the four-point dynamic susceptibility χ_4 ³⁶ and the non-Gaussian parameter α_2 ³⁹. Systems exhibiting stronger dynamical heterogeneity typically show a pronounced long tail in, $G_s(\delta r, t)$ and a double peak structure in $P(\log_{10}(\delta r(t = \tau_\alpha)))$, and both the χ_4 and the α_2 are found to have higher values^{10,13,36,38}. To further probe dynamic variability, we also examine the distribution of particle mobility μ obtained from isoconfigurational ensemble simulations. The mobility distribution, $P(\mu)$ is not identical but similar to the $4\pi\delta r^2 G_s(\delta r, t)$. The former represents an averaged measure of motion over many velocity realizations and thus suppresses some of the heterogeneity captured in the latter. Along with the distribution of μ , we also calculate the distribution of the α -relaxation time from the single particle overlap function, where the overlap function is averaged over the different velocity realizations. In Fig.8 we plot the functions for the LJ system, in Fig.9 we plot the same for the WCA system and in Fig.10 we plot them for the modified LJ

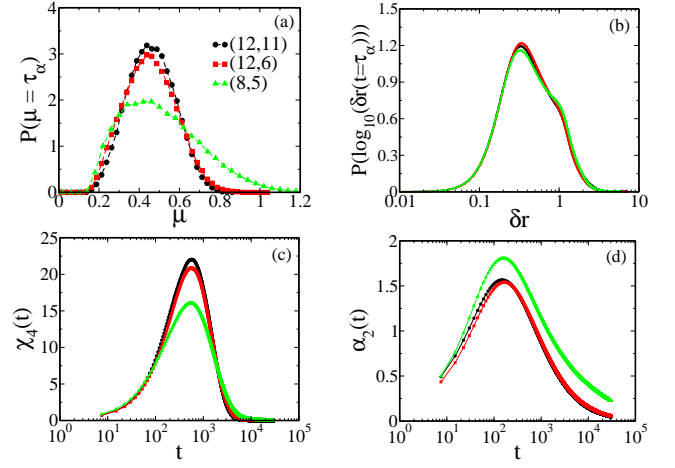


FIG. 10: Different measures of heterogeneity for the modified LJ (q, p) system. (a) Distribution of particle mobilities at the α -relaxation time, obtained from isoconfigurational ensemble simulations. (b) Logarithmic distribution of single-particle displacements, $P(\log_{10}(\delta r(t = \tau_\alpha)))$, derived from standard simulation trajectories. (c) Four-point susceptibility, $\chi_4(t)$, plotted as a function of time. (d) Non-Gaussian parameter, $\alpha_2(t)$, plotted as a function of time. The system exhibiting the maximum structure-dynamics correlation $((8, 5))$ is characterized by a broader $P(\mu)$, a bimodal $P(\log_{10}(\delta r(t = \tau_\alpha)))$, and a higher peak in $\alpha_2(t)$. The color coding in (b), (c), (d) matches that of (a).

(q, p) system.

Our analysis reveals that different measures of dynamic heterogeneity do not necessarily track each other. Interestingly, the systems exhibiting the maximum structure-dynamics correlation, LJ at $\rho = 1.1$ and $(8, 5)$ are both characterized by broader mobility distributions (Fig.8(a) and Fig.10(a)), broader distribution of $P(\tau_\alpha)$ (Fig.14(a) and Fig.14(e) in the Appendix IV), prominent two-peaked structure of $P(\log_{10}(\delta r(t = \tau_\alpha)))$ (Fig.8(b) and Fig.10(b)) and a higher α_2 value (Fig.8(d) and Fig.10(d)). However both these systems show low values of χ_4 (Fig.8(c) and Fig.10(c)). Interestingly, the LJ at $\rho = 1.1$ within its set is the least fragile system but the $(8, 5)$ within its set is the most fragile system. For the LJ system, except for χ_4 no other functions follow fragility, and it is just reverse for the modified LJ (q, p) system where χ_4 does not follow fragility, but all the other functions do. For the WCA system where the change in fragility is the widest, the distribution of mobility $P(\mu)$ (Fig.9(a)) and the α relaxation time $P(\tau_\alpha)$ (Fig.14(c) in the Appendix) are quite similar for all the densities however the other functions, $P(\log_{10}(\delta r(t = \tau_\alpha)))$, α_2 and χ_4 follow fragility.

An important point to note is that, although both the mobility distribution and the single-particle overlap function are derived from the same set of isoconfigurational runs, they are not equivalent. The mobility distribution characterizes the actual displacement of individual particles, whereas the overlap function quantifies the decorrelation of a particle's position, based on whether its displacement exceeds a threshold distance 'a'. However we find that they always correlate.

Another measure of dynamic heterogeneity, the four-point dynamic susceptibility χ_4 is directly related to the fluctuations in the overlap function (Section III C). In the Appendix (see right panels of Fig.14), we plot χ_4 as obtained from isoconfigurational ensemble simulations. Interestingly not the value but the nature of χ_4 obtained from the isoconfigurational run matches with that obtained from regular MD simulation studies which implies that isoconfigurational runs can capture the correlated particle motion. However when compared with the distribution of particle-level relaxation times, $P(\tau_\alpha)$ (see left panels of Fig.14), we find that a broader distribution of $P(\tau_\alpha)$ does not necessarily correspond to larger values of χ_4 . This distinction is crucial: while $P(\tau_\alpha)$ reflects the heterogeneity in relaxation times across individual particles, χ_4 captures how correlated are the dynamics of the particles. Our analysis clearly shows that these two aspects of dynamic heterogeneity are not always aligned.

D. Enthalpy vs entropy contribution

In this section our analysis will shed some light on why the structure-dynamics correlation and distribution of mobility for the two systems (LJ at $\rho = 1.1$ and (8,5)) exhibit similar behaviour, despite having different fragility values. In our previous study involving some of us, we had shown that for an attractive system, the enthalpy, e_{loc} , plays a dominant role, and for a repulsive system, the entropy, S_2 , plays a dominant role in determining the dynamics, and our order parameter can pick up both the contributions⁴⁰. We do a similar analysis for the systems studied here.

In Fig.11(top panels), we plot the overlay between the radial distribution function and the potential for the three sets of systems. We also plot the correlations between different SOPs and the dynamics for the corresponding systems in Fig.11(bottom panels).

We find that for both the LJ and WCA systems, as density increases, the radial distribution function shifts toward lower values of r (Fig.11(a) and Fig.11(b)). In the LJ system, this shift implies that at low density, particles explore the attractive part of the potential, while at high density, they predominantly sample the repulsive part. This transition is reflected in the correlation between local energy, e_{loc} , and dynamics (Fig.11(a)). At $\rho = 1.1$, the system lies in the enthalpy-dominated regime, and as density increases, the correlation between e_{loc} and the dynamics drops sharply. Interestingly, in the high-density regime, where the repulsive part of the potential dominates, the correlation between entropy (S_2) and dynamics becomes strong. Beyond a certain density, however, this correlation plateaus and shows little further variation.

For the WCA system, due to the nature of the potential, particles explore only the repulsive regime at all densities. Consequently, enthalpy exhibits almost no correlation with the dynamics. In contrast, entropy shows a moderate correlation with dynamics, which remains largely unchanged across densities.

In the modified LJ (q, p) system, increasing the softness of the potential results in a broader RDF, allowing particles in softer systems to access more of the attractive part of the potential. As a result, in the (8,5) system, enthalpy plays a dominant role in controlling the dynamics. In contrast, in the (12,11) system, the correlation between e_{loc} and dynamics is weak. We also find that as the potential becomes stiffer,

the systems become increasingly entropy-driven. Notably, our SOP is capable of capturing both entropic and enthalpic contributions to the dynamics.

In Fig.6 (b) where we plot the peak values of the Spearman rank correlation between the SOP and dynamics against the $B/A(\text{micro})$, we find that all the systems which are strongly entropy driven, the WCA systems and LJ systems at $\rho = 1.4$ and $\rho = 1.6$ are all clustered together in the left hand corner of the plot and the enthalpy driven systems are on the right hand corner.

V. CONCLUSION

The main objective of this study is to investigate the relationship between structure-dynamics correlation and fragility in supercooled liquids. Fragility is often associated with enhanced dynamic heterogeneity^{2,12}. Thus, if structural features significantly influence dynamics, one would expect systems with higher fragility to also exhibit stronger structure-dynamics correlation. In a previous study involving some of us, it was shown that the slope of the macroscopic energy barrier, obtained from average dynamics as a function of the structural order parameter (SOP), correlates with fragility²⁰. A more recent study demonstrated that the slope of the microscopic energy barrier, when plotted against a machine-learned softness parameter, also increases with fragility²³. Physically, the slope of the energy barrier versus SOP quantifies how sensitively the barrier, and thus the dynamics, responds to structural changes: a higher slope indicates that even small variations in SOP lead to significant changes in the barrier, reflecting stronger structure-dynamics coupling.

To explore this connection in a general and systematic manner, we consider three distinct sets of model systems: (i) the attractive Lennard-Jones (LJ) system, (ii) the purely repulsive Weeks-Chandler-Andersen (WCA) system, where fragility is tuned by varying density, and (iii) the modified LJ (q, p) system, where fragility is modulated by changing the softness of the interaction potential. This diversity enables us to decouple effects such as density and interaction range from the fragility itself.

Our SOP is observed to vary linearly with temperature, which allows the relaxation time to be fitted in terms of the SOP using a Vogel-Fulcher-Tammann (VFT) form³⁵. The fragility extracted from this SOP-based VFT expression is consistent with the temperature-based fragility. However, a key insight from this analysis is that the slope of the energy barrier as a function of SOP does not necessarily scale with fragility, as often assumed^{23,47}. We also find that the barrier contains a temperature/SOP independent term, which sets the high-temperature limit of the activation energy and affects the slope when unaccounted for. At the macroscopic level, this scaled slope does align with fragility trends. However, at the microscopic level, the relationship is not universal. Notably, an independent and complementary analysis based on isoconfigurational ensemble simulations reveals that the structure-dynamics correlation correlates well with the microscopic scaled slope, reinforcing the idea that high structure-dynamics correlation does not necessarily coincide with high fragility.

We further observe that structure-dynamics correlation is strongest in systems where the dynamics are enthalpy driven.

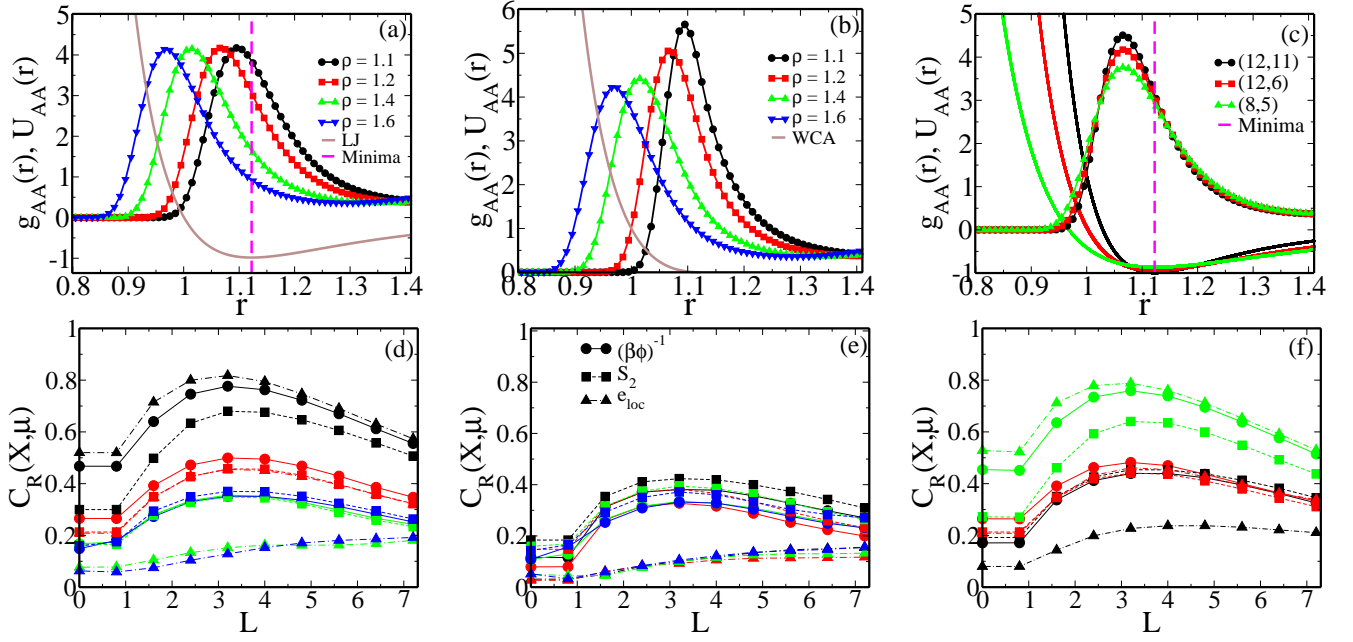


FIG. 11: **Top panels:** Partial radial distribution function, $g_{AA}(r)$, and interparticle potential, $U_{AA}(r)$, plotted as functions of r for three sets of systems: (a) LJ and (b) WCA, each examined at four different densities, and (c) modified LJ (q, p) system. **Bottom panels:** Spearman rank correlation, $C_R((\beta\phi)^{-1}, X)$, between particle mobility, μ , and coarse-grained structural parameters X —where X represents SOP, $(\beta\phi)^{-1}$ (circles), two-body entropy, S_2 (squares), and local energy, e_{loc} (triangles)—plotted as a function of coarse-graining length, L , for the same systems shown in top panels. The color coding in the bottom panels matches that of the top panels.

The systems with the highest correlation are the LJ system at $\rho = 1.1$ and the (8, 5) system, the former is the least fragile within its class, while the latter is the most fragile. Despite this contrast, both systems show broad mobility distributions, bimodal displacement profiles, and high values of the non-Gaussian parameter.

This raises the question of whether enthalpy dominance is intrinsically linked to broad mobility distributions and a form of heterogeneity. Interestingly, both the LJ at $\rho = 1.1$ and the (8, 5) systems lie close to the spinodal line, a regime known to amplify dynamic heterogeneity due to mechanical instability and growing fluctuations²⁷. Although the mechanisms underlying heterogeneity near the spinodal and in supercooled liquids differ, both are characterized by spatially heterogeneous mobility. In systems like (8, 5), high fragility and spinodal proximity may act in tandem to produce pronounced dynamical heterogeneity.

In conclusion, our findings reveal that fragility and structure-dynamics correlation do not always correlate. While fragility has often been associated with increased dynamic heterogeneity, our study shows that this relationship is more nuanced. Importantly, dynamic heterogeneity must be evaluated using a broader set of metrics beyond the commonly used four-point susceptibility, which captures spatially correlated motion. We find that the breadth of mobility distributions, such as those obtained from isoconfigurational ensemble simulations, is often a more sensitive indicator of the structural influence on dynamics than χ_4 . This perspective broadens our understanding of the

glass transition and underscores the necessity of employing multiple, complementary measures when exploring the complex interplay between structure, dynamics, and fragility in supercooled liquids.

Appendix I: Structural Order Parameter at Macroscopic and Microscopic Levels

In a binary system, at the microscopic level, the effective caging potential experienced by particle i of type u is given by

$$\beta\phi_u^i = -\rho \int dr \sum_v x_v C_{uv}^i(r) g_{uv}^i(r), \quad (23)$$

where ρ is the number density, $C_{uv}^i(r)$ is the local direct correlation function, and $g_{uv}^i(r)$ is the local radial distribution function for particle i . We work with the absolute value of the caging potential and the SOP which is the inverse of the depth of the caging potential, is given by,

$$SOP = (\beta\phi_u^i)^{-1} = 1 / \left(\rho \int dr \sum_v x_v C_{uv}^i(r) g_{uv}^i(r) \right) \quad (24)$$

This gives rise to a distribution of the SOP²². The aver-

age of this distribution can be written as,

$$\begin{aligned} \langle (\beta\phi_u^i)^{-1} \rangle &= \left\langle \frac{1}{\rho} \int dr \sum_v x_v C_{uv}^i(r) g_{uv}^i(r) \right\rangle_i \\ &= \frac{1}{\rho} \int dr \sum_v \langle C_{uv}^i(r) g_{uv}^i(r) \rangle x_v \end{aligned} \quad (25)$$

Although the macroscopic and microscopic SOP have the same functional forms, it is important to note that since the SOP is a nonlinear function of the radial distribution function, the average of the microscopic SOP is quantitatively not the same as the macroscopic SOP (Eq.3). Although $\langle g_{uv}^i(r) \rangle = g_{uv}(r)$, $\langle C_{uv}^i(r) g_{uv}^i(r) \rangle \neq C_{uv}(r) g_{uv}(r)$, i.e., the average of a product is not equal to the product of averages. As a result, the macroscopic SOP $(\beta\Phi)^{-1}$ and microscopic average SOP $\langle (\beta\phi)^{-1} \rangle$ have different values but interestingly similar trend as seen in right panels of Fig.2.

To maintain consistency and avoid unphysical contributions in the microscopic calculations, particularly at small r , we adopt an approximation for the direct correlation function. This has been discussed in detail in earlier studies^{40,48}. Specifically, we replace the HNC expression with a simplified form:

$$C_{uv}^{\text{approx}}(r) = g_{uv}(r) - 1, \quad (26)$$

and use this same approximation consistently in both macroscopic and microscopic calculations. We present the temperature dependence of the SOP for all three sets of systems studied (LJ, WCA, and modified LJ (q, p) system). In the right panes of Figure 2 we show that both $1/(\beta\Phi)$ and $\langle 1/(\beta\phi) \rangle$ exhibit a linear dependence on temperature across all systems. This observation is consistent with earlier studies^{20,22}. As discussed before, although the absolute values of the order parameters differ between the macroscopic and microscopic levels, their trends are similar.

Appendix II: Identification of Fast Particles and Calculation of Microscopic Activation Energy

To identify dynamically fast particles and calculate their microscopic activation energy, we follow the method introduced by Candelier et al.^{49,50}. This approach allows us to detect cage rearrangements by analyzing particle trajectories in a fixed time window. For each particle i at time t , a hopping propensity $p_{\text{hop}}(i, t)$ is computed over a window $W = [t_1, t_2]$ using the expression:

$$p_{\text{hop}}(i, t) = \sqrt{\langle (\vec{r}_i - \langle \vec{r}_i \rangle_U)^2 \rangle_V \langle (\vec{r}_i - \langle \vec{r}_i \rangle_V)^2 \rangle_U}, \quad (27)$$

where the time intervals $U = [t - \Delta t/2, t]$ and $V = [t, t + \Delta t/2]$ represent regions before and after time t , respectively. In our calculations, we use $\Delta t = 15\tau$. A low p_{hop} value indicates the particle is localized within a cage,

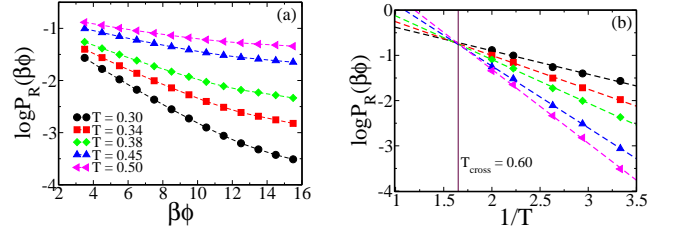


FIG. 12: (a) Plot of $\log P_R$ as a function of inverse structural order parameter, $\beta\phi$, at various temperatures. (b) Plot of $\log P_R$ versus inverse temperature $1/T$ for several fixed ($\beta\phi$) values. Each curve corresponds to a different inverse SOP (i.e., ($\beta\phi$)) value, with black representing low inverse SOP values and magenta representing high inverse SOP values. The vertical solid line indicates the temperature at which all curves intersect, and this cross temperature is the onset temperature for all systems^{19,22}.

whereas a high value signifies a cage jump. To determine a threshold p_c for identifying rearranging particles, we use the value of mean square displacement (MSD) at which the non-Gaussian parameter $\alpha_2(t)$ attains its maximum⁵¹. The formal definition of $\alpha_2(t)$ is provided in Section III D, and the corresponding time is used to set the relevant rearrangement scale. Any particle i with $p_{\text{hop}}(i, t) > p_c$ is categorized as dynamically fast and said to undergo a rearrangement at time t . We then analyze the correlation between structure and dynamics using the probability of rearrangement, P_R , as a function of the inverse SOP. We denote this probability as $P_R(\beta\phi)$, where $\beta\phi$ represents the inverse of the SOP for a given particle. In Fig.12(a), we plot $P_R(\beta\phi)$ versus ($\beta\phi$) for different temperatures. At high temperatures, the curves appear flat, indicating that rearrangement is nearly independent of local structure. However, at lower temperatures, a clear dependence emerges—particles with smaller $\beta\phi$ values are significantly more likely to rearrange.

To extract the microscopic activation energy, we analyze the temperature dependence of the rearrangement probability for fixed SOP values. Specifically, we fit $P_R(\beta\phi)$ as a function of inverse temperature $1/T$ for several values of ($\beta\phi$) using the Arrhenius form:

$$P_R(\beta\phi) = P_0(\beta\phi) \exp \left[-\frac{\Delta E(\beta\phi)}{T} \right], \quad (28)$$

where $\Delta E(\beta\phi)$ is interpreted as the microscopic activation energy required for rearrangement and depends on the local structure via ($\beta\phi$). This is shown in Fig.12(b), which demonstrate the increasing structural control over dynamics at lower temperatures. This method thus establishes a direct quantitative link between local structural features and the energy barrier for particle rearrangements.

Appendix III: Macroscopic Activation En-

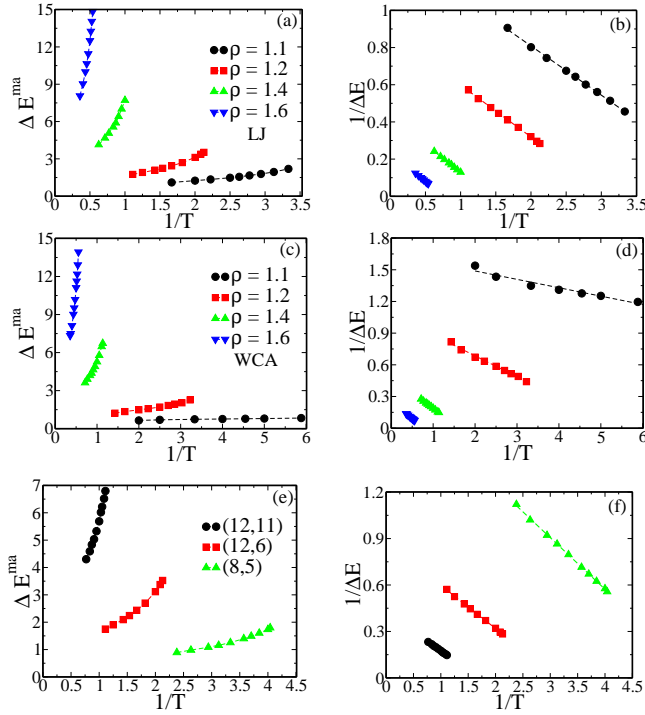


FIG. 13: **Left panels:** Variation of the macroscopic activation energy ΔE^{ma} with inverse temperature $1/T$ for three sets of systems: (a)LJ and (c)WCA, each examined at four different densities, and (e) modified LJ (q, p) system. **Right panels:** The inverse activation energy, $1/\Delta E^{ma}$, is plotted against $1/T$ for the same systems. The slope of the resulting linear fits provides the fragility, K_{VFT} as shown in Eq.20. The corresponding values are listed in Table I. The color coding in the right panels matches that of the left panels.

ergy as a function of Temperature

To support the fragility analysis discussed in the main text, we present additional plots here that clarify the underlying trends for all three sets of systems: LJ, WCA, and modified LJ (q, p) system. In the left panels of Fig.13, we show ΔE^{ma} plotted against $1/T$. These plots reflect how activation energy varies with temperature and how its slope correlates with the system's fragility. As mentioned in the main text, for LJ and WCA systems, increasing density results in higher T_{VFT} and fragility, accompanied by an increase in the slope of ΔE^{ma} vs $1/T$. In contrast, among the modified LJ (q, p) system, (8,5) exhibits the highest fragility but the lowest T_{VFT} , resulting in the smallest slope. In the right panels of Fig.13, we show the corresponding plots of $1/\Delta E^{ma}$ versus $1/T$. The slopes of these linear fits yield the fragility, K_{VFT} , which exactly matches the fragility values obtained from the VFT fit of the relaxation time using Eq.11. The extracted values are listed in Table I.

TABLE II: Slope (B') and intercept (A') values from the linear fit of $\frac{1}{\Delta E^{ma}}$ vs. $1/\Delta((\beta\Phi)^{-1})$ (right panels of Fig.1), and slope ($B(micro)$) and intercept ($A(micro)$) values from the fit of ΔE vs. $1/\Delta((\beta\phi)^{-1})$ (left panels of Fig.5). The corresponding values for each system are listed in the table.

System	A'	B'	$A(micro)$	$B(micro)$
LJ, $\rho = 1.1$	1.320	0.0177	0.528	0.146
LJ, $\rho = 1.2$	0.869	0.0123	1.968	0.198
LJ, $\rho = 1.4$	0.426	0.0066	5.654	0.395
LJ, $\rho = 1.6$	0.234	0.0038	11.99	0.784
WCA, $\rho = 1.1$	1.614	0.0057	0.501	0.033
WCA, $\rho = 1.2$	1.067	0.0098	1.352	0.117
WCA, $\rho = 1.4$	0.486	0.0070	4.632	0.321
WCA, $\rho = 1.6$	0.251	0.0039	10.50	0.822
(12, 11)	0.425	0.0052	3.815	0.360
(12, 6)	0.948	0.0143	2.030	0.196
(8, 5)	1.893	0.0368	0.827	0.124

Appendix IV: Structure-Dynamics Correlation: Isoconfigurational Ensemble and Rank Analysis

To investigate the correlation between structure and dynamics in our system, we use the isoconfigurational ensemble method introduced by Harrowell et al.¹⁸. In this method, an ensemble of trajectories is generated from the same initial configuration of particles, with initial velocities drawn randomly from the Maxwell-Boltzmann distribution at the corresponding temperature. This approach eliminates trivial variations in dynamics due to different initial momenta, allowing us to assess the role of structural features in determining the dynamics.

In our study, we use 32 different initial configurations, each separated by at least $75\tau_\alpha$ to ensure statistical independence. From each configuration, we generate 100 trajectories with randomised initial momenta. The dynamics of each particle are quantified by its mobility, defined as:

$$\mu^j(t) = \frac{1}{N_{IC}} \sum_{i=1}^{N_{IC}} \left| \mathbf{r}_i^j(t) - \mathbf{r}_i^j(0) \right|, \quad (29)$$

where $\mu^j(t)$ is the average displacement of the j^{th} particle over N_{IC} isoconfigurational trajectories at time t . We have also calculated the per-particle α -relaxation time by averaging over 200 isoconfigurations for each particle. In the left panels of Fig.15, we present the distribution of the per-particle α -relaxation times. We find that the distribution of mobility and relaxation time show similar behaviour.

In right panels of Fig.14, we plot χ_4 as obtained from isoconfigurational ensemble simulations. Interestingly, not the value but the nature of χ_4 obtained from the isoconfigurational run matches with that obtained from regular MD simulation studies, which implies that isoconfigurational runs can capture the correlated particle

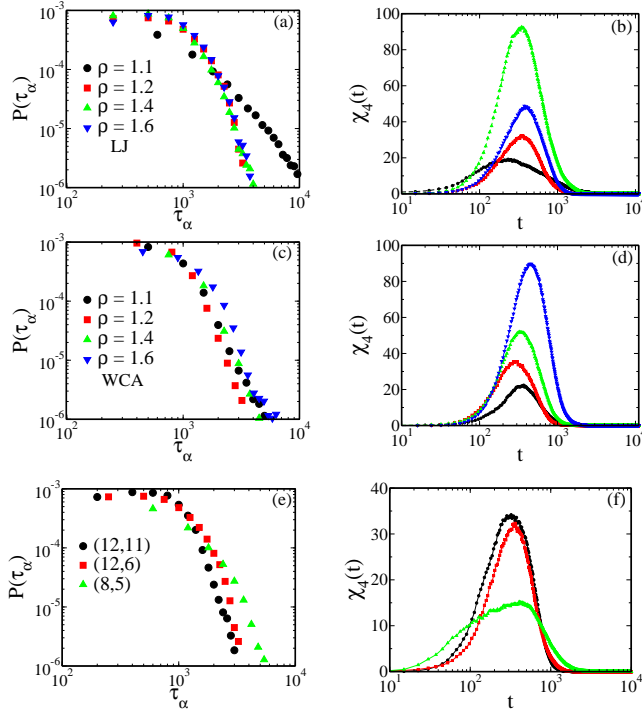


FIG. 14: **Left panels:** Distribution of per-particle α -relaxation times obtained from isoconfigurational ensemble simulations for three sets of systems: (a) LJ and (c) WCA, each examined at four different densities, and (e) modified LJ (q, p) system. **Right panels:** Corresponding four-point susceptibility, $\chi_4(t)$, plotted as a function of time for the same systems shown in the left panels. The color coding in the right panels matches that of the left panels.

motion. However, when compared with the distribution of particle-level relaxation times, $P(\tau_\alpha)$ (see left panels of Fig.14), we find that a broader distribution of $P(\tau_\alpha)$ does not necessarily correspond to larger values of χ_4 . This distinction is crucial: while $P(\tau_\alpha)$ reflects the heterogeneity in relaxation times across individual particles, χ_4 captures how correlated the dynamics of the particles are. Our analysis clearly shows that these two aspects of dynamic heterogeneity are not always aligned.

To quantify the correlation between structural parameters (such as the SOP) and dynamics (such as mobility), we use the Spearman rank correlation coefficient. Given m data points $\{X_i\}$ and $\{Y_i\}$, the Spearman coefficient is defined as:

$$C_R(X, Y) = 1 - \frac{6 \sum_{i=1}^m d_i^2}{m(m^2 - 1)}, \quad (30)$$

where $d_i = R(X_i) - R(Y_i)$ is the difference in ranks of the i^{th} values of variables X and Y .

This correlation coefficient is used to assess how well the SOP of particles in the initial configuration correlates with their mobility at later times. A strong (positive

or negative) correlation indicates that the structure of a particle's local environment significantly influences its dynamic behavior.

To demonstrate that the qualitative nature of the structure-dynamics correlation for different systems is not specific to any particular choice of L , we show in the left panels of Fig.15 the same correlations as presented in Fig.7 but calculated at a fixed $L = 1$. The similar trends observed across densities confirm that our findings are robust and do not depend sensitively on the choice of L . The right panels of Fig.15 shows the Spearman rank correlation, $C_R((\beta\phi)^{-1}, X)$, between the SOP, $(\beta\phi)^{-1}$, and both mobility, μ , calculated at α -relaxation time and per-particle level α -relaxation time. Both correlations exhibit similar trends.

TABLE III: The working temperature, T , is selected for each system to ensure that the α -relaxation times are comparable across different densities. This choice facilitates a consistent comparison of structural-dynamic correlations and dynamic heterogeneity analyses among the various systems studied.

System	T
LJ, $\rho = 1.1$	0.30
LJ, $\rho = 1.2$	0.47
LJ, $\rho = 1.4$	1.00
LJ, $\rho = 1.6$	1.85
WCA, $\rho = 1.1$	0.134
WCA, $\rho = 1.2$	0.31
WCA, $\rho = 1.4$	0.88
WCA, $\rho = 1.6$	1.78
(12, 11)	0.90
(12, 6)	0.47
(8, 5)	0.2475

ACKNOWLEDGMENT

S. M. B. thanks, Science and Engineering Research Board (SERB, Grant No. SPF/2021/000112) for the funding. SS acknowledges support through the JC Bose Fellowship (JBR/2020/000015) from the Science and Engineering Research Board, Department of Science and Technology, India. S. M. B. would like to thank Sanat Kumar and Indrajit Tah for discussions. M. S. acknowledges CSIR for the research fellowships.

AVAILABILITY OF DATA

The data that support the findings of this study are available from the corresponding author upon reasonable request.

VI. REFERENCES

¹P. G. Debenedetti and F. H. Stillinger, Nature **410**, 259 (2001).

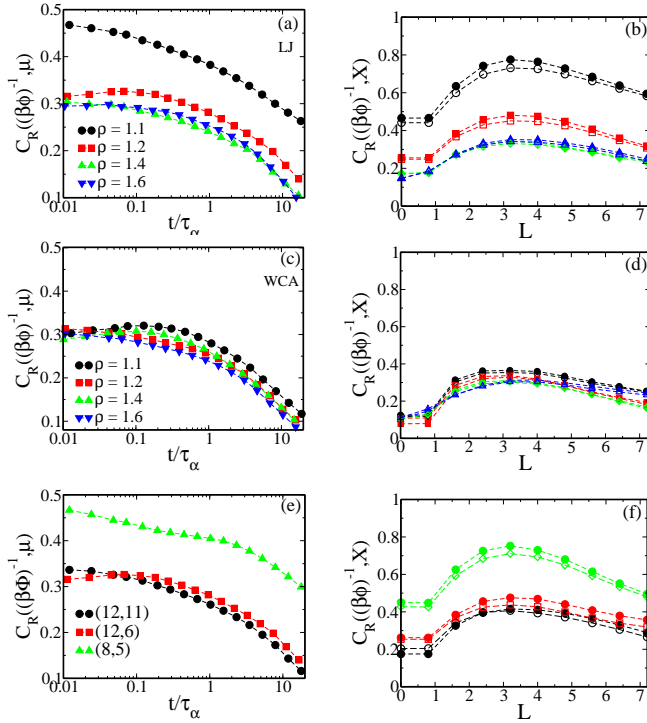


FIG. 15: **Left panels:** Spearman rank correlation, $C_R((\beta\phi)^{-1}, \mu)$, between the SOP, $(\beta\phi)^{-1}$, and mobility, μ , computed at $L = 1$ for three different sets of systems: (a) LJ and (c) WCA, each examined at four different densities, and (e) modified LJ (q, p) system. This figure complements the main results shown in Fig. 7, and demonstrates that the observed density-dependent behavior is not sensitive to the choice of L . **Right panels:** Spearman rank correlation, $C_R((\beta\phi)^{-1}, X)$, between the SOP, $(\beta\phi)^{-1}$, and the dynamic quantity X , where X represents either the instantaneous mobility μ evaluated at the α -relaxation time (closed symbols) or the particle-level α -relaxation times averaged over 200 isoconfigurational ensembles (open symbols) for the same systems shown in left panels. The color coding in the right panels matches that of the left panels.

- ²M. D. Ediger, Annual Review of Physical Chemistry **51**, 99 (2000).
³J. C. Dyre, Reviews of Modern Physics **78**, 953 (2006).
⁴V. Lubchenko and P. G. Wolynes, Annual Review of Physical Chemistry **58**, 235 (2007).
⁵H. Tong and H. Tanaka, Physical Review X **8**, 011041 (2018).
⁶C. A. Angell, Science **267**, 1924 (1995).
⁷L. M. Martinez and C. A. Angell, Nature **410**, 663 (2001).
⁸H. Sillescu, Journal of Non-Crystalline Solids **243**, 81 (1999).
⁹C. Donati, S. C. Glotzer, P. H. Poole, W. Kob, and S. J. Plimpton, Physical Review E **60**, 3107 (1999).
¹⁰W. Kob, C. Donati, S. J. Plimpton, P. H. Poole, and S. C. Glotzer, Physical Review Letters **79**, 2827 (1997).
¹¹G. Biroli, J.-P. Bouchaud, K. Miyazaki, and D. R. Reichman, Physical Review Letters **97**, 195701 (2006).

- ¹²S. Sastry, Nature **409**, 164 (2001).
¹³N. Lacey, F. W. Starr, T. B. Schroder, and S. C. Glotzer, The Journal of Chemical Physics **119**, 7372 (2003).
¹⁴C. Toninelli, G. Biroli, and D. S. Fisher, Physical Review E **71**, 041505 (2005).
¹⁵A. Banerjee, S. Sengupta, S. Sastry, and S. M. Bhattacharyya, Physical Review Letters **113**, 225701 (2014).
¹⁶A. Banerjee, M. K. Nandi, S. Sastry, and S. M. Bhattacharyya, The Journal of Chemical Physics **145**, 034502 (2016).
¹⁷M. K. Nandi, A. Banerjee, S. Sengupta, S. Sastry, and S. M. Bhattacharyya, The Journal of Chemical Physics **143**, 174504 (2015).
¹⁸A. Widmer-Cooper, H. Perry, P. Harrowell, and D. R. Reichman, Nature Physics **4**, 711 (2008).
¹⁹S. S. Schoenholz, E. D. Cubuk, D. M. Sussman, E. Kaxiras, and A. J. Liu, Nature Physics **12**, 469 (2016).
²⁰M. K. Nandi and S. M. Bhattacharyya, Physical Review Letters **126**, 208001 (2021).
²¹D. Richard et al., Physical Review Materials **4**, 113609 (2020).
²²M. Sharma, M. K. Nandi, and S. M. Bhattacharyya, Physical Review E **105**, 044604 (2022).
²³I. Tah, S. A. Ridout, and A. J. Liu, The Journal of Chemical Physics **157**, 124501 (2022).
²⁴L. Berthier and G. Tarjus, The Journal of Chemical Physics **134**, 214503 (2011).
²⁵S. Sengupta, F. Vasconcelos, F. Affouard, and S. Sastry, The Journal of Chemical Physics **135**, 194503 (2011).
²⁶P. Bordat, F. Affouard, M. Descamps, and K. L. Ngai, Physical Review Letters **93**, 105502 (2004).
²⁷V. Testard, L. Berthier, and W. Kob, The Journal of Chemical Physics **140**, 164502 (2014).
²⁸W. Kob and H. C. Andersen, Physical Review Letters **73**, 1376 (1994).
²⁹J. D. Weeks, D. Chandler, and H. C. Andersen, The Journal of Chemical Physics **54**, 5237 (1971).
³⁰D. L. Majure et al., Large-scale atomic/molecular massively parallel simulator (lammmps) simulations of the effects of chirality and diameter on the pullout force in a carbon nanotube bundle, in Proceedings of the HPCMP Users Group Conference 2008, pp. 201–207, 2008.
³¹T. V. Ramakrishnan and M. Yussouff, Physical Review B **19**, 2775 (1979).
³²J.-P. Hansen and I. R. McDonald, Theory of Simple Liquids, 4th ed. (Academic Press, 2013).
³³P. M. Piaggi, O. Valsson, and M. Parrinello, Physical Review Letters **119**, 015701 (2017).
³⁴T. Goel, C. N. Patra, T. Mukherjee, and C. Chakravarty, The Journal of Chemical Physics **129**, 164904 (2008).
³⁵L. S. García-Colín, L. F. del Castillo, and P. Goldstein, Physical Review B **40**, 7040 (1989).
³⁶E. Flenner, H. Staley, and G. Szamel, Physical Review Letters **112**, 097801 (2014).
³⁷L. van Hove, Physical Review **95**, 249 (1954).
³⁸J.-L. Barrat, J. Baschnagel, and A. V. Lyulin, Soft Matter **6**, 3430 (2010).
³⁹A. Rahman, Physical Review **136**, A405 (1964).
⁴⁰M. Sharma, M. K. Nandi, and S. M. Bhattacharyya, The Journal of Chemical Physics **159**, 104502 (2023).
⁴¹H. Tong and H. Tanaka, Nature Communications **10**, 5596 (2019).
⁴²H. Tong and H. Tanaka, Physical Review Letters **124**, 225501 (2020).
⁴³B. Mei, B. Zhuang, Y. Lu, L. An, and Z. Wang, Journal of Physical Chemistry Letters **13**, 3957 (2022).
⁴⁴Y. Qiu, I. Jang, X. Huang, and A. Yethiraj, Proceedings of the National Academy of Sciences **122**, e2427246122 (2025).
⁴⁵H. Tanaka, Journal of Physical Chemistry B **129**, 789 (2025).
⁴⁶E. Flenner and G. Szamel, Physical Review E **72**, 031508 (2005).
⁴⁷M. K. Nandi, A. Banerjee, C. Dasgupta, and S. M. Bhattacharyya, Physical Review Letters **119**, 265502 (2017).

- ⁴⁸P. Patel, M. Sharma, and S. M. Bhattacharyya, The Journal of Chemical Physics **159**, 044501 (2023).
- ⁴⁹R. Candelier et al., Physical Review Letters **105**, 135702 (2010).
- ⁵⁰A. Smessaert and J. Rottler, Physical Review E **88**, 022314 (2013).
- ⁵¹F. P. Landes, G. Biroli, O. Dauchot, A. J. Liu, and D. R. Reichman, Physical Review E **101**, 010602 (2020).